Exploration of new chiral hybrid semiconducting palladium halide complexes: [(R)/(S)-2-Methylpiperazinediium]PdCl4

Fadhel Hajlaoui, Bochra Ben Salah, Karim Karoui, Nathalie Audebrand, Thierry Roisnel, Nabil Zouari, Fathi Jomni

To cite this version:

Fadhel Hajlaoui, Bochra Ben Salah, Karim Karoui, Nathalie Audebrand, Thierry Roisnel, et al.. Exploration of new chiral hybrid semiconducting palladium halide complexes: [(R)/(S)-2-Methylpiperazinediium]PdCl4. Materials Research Bulletin, 2023, 164, pp.112251. 10.1016/j.materresbull.2023.112251 . hal-04115714

HAL Id: hal-04115714

https://hal.science/hal-04115714v1

Submitted on 12 Jun 2023

Highlights

- (R)/(S)-2-methylpiperazine were used in the synthesis of chiral Pd(II)-hybrid halide complexes [(R)-$C_5H_{14}N_2$]$PdCl_4$ and [(S)-$C_5H_{14}N_2$]$PdCl_4$.
- Two structures were determined using single-crystal X-ray diffraction and both of them are lucky to crystallize in chiral space group $P2_12_12_1$.
- The semiconductor properties of hybrid materials are identified by the optical and electrical studies.

Exploration of New Chiral Hybrid Semiconducting Palladium Halide Complexes: [(R)/(S)-2-Methylpiperazinediium]$PdCl_4$

Bochra Ben Salah [a], Fadhel Hajlaoui*[b], Karim Karoui [c, d], Nathalie Audebrand [e], Thierry Roisnel [e], Stéphane Freslon [e], Nabil Zouari [b], Fathi Jomni [f].

[a] Laboratory of Medicinal and Environmental Chemistry, Higher Institute of Biotechnology of Sfax, University of Sfax, 3018 Sfax, Tunisia

[b] Laboratoire Physico-chimie de l'Etat Solide, Département de Chimie, Faculté des Sciences de Sfax, B.P. 1171, 3000 Sfax, Université de Sfax, Tunisia

[c] Laboratoire des caractérisations spectroscopiques et optique des matériaux, Faculté des Sciences de Sfax, B.P. 1171, 3000 Sfax, Université de Sfax, Tunisia

[d] Greman UMR 7347-CNRS, CEA, INSACVL, University of Tours, Blois, France

[e] Univ Rennes, CNRS, INSA Rennes, ISCR (Institut des Sciences Chimiques de Rennes) - UMR 6226, F-35000 Rennes, France

[f] Université de Tunis El Manar, Laboratoire LMOP, LR99ES17, El Manar, 2092 Tunis, Tunisia

**Corresponding Authors' E-mail: fadhelh83@yahoo.fr*

Abstract

Chiral organic-inorganic halogenometallate hybrids have attracted significant research interest in various fields from optoelectronic to photovoltaic devices. However, to this day the range of available chiral hybrid metal halides still remains limited. In this context, single crystals of organically templated chiral chloropalladate (II), [(R)/(S)-$C_5H_{14}N_2$]$PdCl_4$, have been synthesized. Each of the chiral molecular compound consists of (R) or (S)-2-methylpiperazinediium $[C_5H_{14}N_2]^{2+}$ cations and $[PdCl_4]^{2-}$ anions. The complexes, [(R)/(S)-$C_5H_{14}N_2$]$PdCl_4$ crystallize in the chiral space group $P2_12_12_1$ (No. 19), which exhibits the enantiomorphic crystal class 222 (*D*2). In the crystal structure, the $[PdCl_4]^{2-}$ anions are linked to the organic cations through N-H···Cl and C-H···Cl hydrogen bonds to form cation-anion-cation molecular units. The incorporation of a protonated (R) or (S)-2-methylpiperazine cations into the same inorganic halide systems leads to similar properties. The thermal analysis, optical and electric properties of [(R)-$C_5H_{14}N_2$]$PdCl_4$ (1) compound have been studied. The title compound [(R)-$C_5H_{14}N_2$]$PdCl_4$ (1) reveals thermal stability up to ca. 450 K. Besides, [(R)-$C_5H_{14}N_2$]$PdCl_4$ (1) shows semiconducting behavior with an optical band gap of ~3.64

eV. The electric properties are investigated and the equivalent circuit is chosen and confirms the contribution of the grain and grain boundaries. The values of AC conductivities (10^{-6} $\Omega^{-1}cm^{-1}$) confirm the gap energy and the semiconducting character of the R enantiomer. The value of activation energy is determinated and shows the ionic conduction type. Such a chiral hybrid metal halide offers a viable strategy for the targeted design and synthesis of non-centrosymmetric metal halide materials for optoelectronic applications.

Keywords

Chiral halogenometallate, Enantiomorphic crystal, Semiconducting behaviour, Electric properties.

1. Introduction

Organic-inorganic halogenometallate hybrids are an important class of crystalline materials with especial structural and diverse range of physical properties such as photovoltaic activity **[1]**, luminescence **[2-4]**, optoelectronic **[5]**, ferromagnetism **[6]** and ferroelectricity **[7]**. Crystal structures of some of these compounds can be regarded as derived from the cubic perovskite AMX_3 along vertices of the MX_6 octahedra with additional moieties inserted between these layers, where the M atom is typically a metal cation and X is an anion (Cl^-, Br^- or I^-). The label A is assigned to an organic cation, filling the space enclosed by MX_6 octahedra and balancing the charge of the whole network. It was previously concluded that halogenometallate hybrid materials are able to associate properties from both the organic and inorganic structural components and possess greater functionality than the components on their one **[8]**. Hybrid metal halides attract considerable attention due to their tunable structures, which can vary from 0 D to three-dimensional, and their attractive optical and electronic properties, such as tunable optical bandgaps, circular dichroism, high optical absorption and excellent charge transport **[9-11]**.

Currently, investigations of such halogenometallate hybrid materials have been greatly expanded **[12]**. Among them, two conventional families are commonly defined in terms of their generic stoichiometries AMX_4 and A_2MX_4, respectively, in which MX_4 can adopt a tetrahedral or square planar geometry. A number of examples show that these materials can possess luminescence properties that vary from sharp lines to broad white light emission **[13]**. They can also be used in applications such as solar cells and lasers and show greater thermal stability than their AMX_3 hybrid perovskite parent compounds **[14-15]**. Additionally, they provide great opportunities and open a new domain of materials design. Thus, the variation of organic cations and halogen atoms allows to adjust the band-gap width of hybrid metal halides and to obtain semiconductor materials **[16]**. Furthermore, the range of properties of these materials is remarkably increased when they adopt chiral structures **[17-18]**.

There are several ways in which materials can obtain chiral crystal structures: amino acids are among the sources of chirality and are very suitable building blocks for incorporation into halogenometallate hybrid structures **[19-20]**. For instance, Mercier et al. incorporated chiral α-amino acids lysine and ornithine into a hybrid lead halide perovskite structure. This resulted in novel 1D perovskite-like materials which displays unprecedent dual phosphorescence emission properties **[21]**. Additionally, in the work reported by Heindl et al. introducing enantiomerically-pure 3- aminobutyric acid (3- ABA) into thin films of the 1D semiconductor dimethylammonium lead iodide ($DMAPbI_3$) results in strong circular dichroism in the optical absorption **[22]**. However, despite the promising properties of chiral hybrid metal halides, this domain is still only at the beginning of its development and the examples of chiral halogenometallate hybrids are quite limited. One of the key tasks for nowadays is the synthesis of new chiral halogenometallate hybrids starting from simple and easily accessible reagents. Indeed, the incorporation of a pure enantiomeric chiral organic amine in metal halides is the most attractive way to create chiral materials. These can be used in a wide range of applications such as nonlinear optical responses **[23-25]**, ferroelectricity **[26-27]**, smart optoelectronic **[28]** and spintronics materials **[29]**.

The beginning of the field of chiral hybrid metal halides can be attributed to the publications of Billing et al.: the incorporation of the enantiomeric chiral amine (S)-methylbenzylammonium ((S)-MBA), was reported in 2003 **[30]**. Structurally, $[(R)/(S)\text{-}MBA]PbX_3$ (X = Cl, Br or I) exhibit 1D face-sharing structures, whereas $[(R)/(S)\text{-}MBA]_2PbI_4$ exhibit 2D corner-sharing layered structures **[30]**. **Numerous hybrid metal halides have been recently characterized including zero-dimensional (0D) materials. For example, $[(R)/(S)\text{-}MBA)_4Bi_2I_{10}]$ perovskite derivative structure show a structural chirality transfer to the organic–inorganic interface, wherein the enantiopure chiral amines induce symmetry-breaking helical distortions in the inorganic framework via asymmetric hydrogen bonding interactions. Consequently, optical properties like circular dichroism (CD), second harmonic generation and circularly polarized luminescence are observed [30].**

Chiral hybrid metal halides compounds were then extended to new chiral amines such as, (R)-3-ammoniopiperidin-1-ium (3-APD) **[31]**, (R)/(S)-1-(1-naphthyl)ethylammonium (NEA) **[32]** and (R)/(S)-1-(4-chlorophenyl)ethylammonium **[33]**. As a result of introducing chiral source, the compounds $[(R)\text{-}3\text{-}APD]PbCl_4{\cdot}H_2O$, $[(R)/(S)\text{-}NEA]_2Pb_4Cl_{10}{\cdot}2DMF$, **$[(R)/(S)\text{-}NEA]_2PbBr_4$** $[(R)/(S)\text{-}ClC_6H_4CH(NH_3)CH_3]_2PbI_4$ exhibit interesting optoelectronic and ferroelectric properties **[33]**.

In the same way, the development of lead-free chiral hybrid halide materials that exhibit multiple physical properties has attracted widespread attention. For instance, the hybrid halometallate compounds $((R)/(S)\text{-}3\text{-chloro-}2\text{-hydroxypropyltrimethylammonium})_2CuCl_4$ show switching properties in seven physical channels: dielectricity, conductivity, second harmonic generation (SHG), piezoelectricity, ferroelasticity, chirality, and thermochromism **[34]**. Additionally, ((R)-(-)-

3-hydroxyquinuclidium)$FeCl_4$ was synthetized. Indeed, the use of chiral cation can help in achieving a ferroelectric compound with ferroelastic behavior in a wide range of temperatures **[35]**. Interestingly, the structural arrangement remains similar for either (R) or (S) chiral versions of these hybrid compounds, thereby enabling a well-defined comparison of the impact of chirality **[36]**. Thus, the incorporation of a diprotonated (R) or (S)-2-methylpiperazine cations into inorganic metal halide leads to **the development of excellent optical materials with good thermal stability [37]**. **Guided by the above cognition, we focused on a combination of chiral organic cations [(R)/(S)-$C_5H_{14}N_2$]$^{2+}$, the d^8 cation Pd^{2+} and halide anions Cl$^-$, which leads to the synthesis of one pair of chiral hybrid semiconducting palladium halides, [(R)/(S)-$C_5H_{14}N_2$]$PdCl_4$.** For the compound [(R)-$C_5H_{14}N_2$]$PdCl_4$ (1) thermal analysis, optical activity and electric properties are provided and studied.

2. Experimental section

2.1.Materials

Palladium(II) chloride ($PdCl_2$), hydrochloric acid (HCl 37%), (R)-(−)-2-methylpiperazine ((R)-$C_5H_{12}N_2$), (S)-(+)-2-methylpiperazine ((S)-$C_5H_{12}N_2$) were purchased from Sigma-Aldrich and used without further purification. Deionized water was used in these syntheses.

2.2.Synthesis of [(R)-$C_5H_{14}N_2$]$PdCl_4$ (1) and [(S)-$C_5H_{14}N_2$]$PdCl_4$ (2)

At room temperature, single crystals of [(R)-$C_5H_{14}N_2$]$PdCl_4$ (1) and [(S)-$C_5H_{14}N_2$]$PdCl_4$ (2) were grown by slow evaporation from aqueous solution of HCl, [(R) or (S)-$C_5H_{12}N_2$] and $PdCl_2$ in the 1/2/1 molar ratio. Orange prismatic crystals were observed after few days for each reaction. Reaction yield ranges between 71-88%, base Pd.

2.3. Elemental Analysis

Scanning Electronic Microscopy (SEM) and Energy-Dispersive Spectroscopy (EDS) measurements have been performed with a Hitachi TM-1000 Tabletop Microscope version 02.11 with EDS analysis system, which were typically operated at 15 KV. All EDS measurements were performed several times on several particles in order to insure reproducibility and to confirm the powders chemical homogeneity. The SEM observations and the EDX analysis of compounds (**1**) and (**2**) are shown in figure S3. The atomic percentage of palladium and chlorine are tabulated in inset of each figure, which confirms the elemental composition of metal and halides.

2.4.Infrared spectroscopy

Infrared measurements were obtained using a Perkin-Elmer FTIR Spectrometer as KBr pellets in the range 4000-400 cm^{-1}. **The FTIR spectra in figures S1, S2; tables S4 and S5 further confirm the presence of the [$C_5H_{14}N_2$]$^{2+}$ cations. The broad band around 3360 cm^{-1} belongs to the N-H stretching peak. The bands in the range of 2940–2830 cm^{-1} are assigned to the CH_2 and CH_3**

symmetric and asymmetric stretching vibrations and the band around 1415 cm^{-1} is ascribed to C–H bending vibrations. The bands seen at 965 cm^{-1} and 850 cm^{-1} are attributed to δ(C-N).

2.5. Single-crystal data collection and structure determination

Single-crystal X-ray diffraction data of $[(R)\text{-}C_5H_{14}N_2]PdCl_4$ (**1**) and $[(S)\text{-}C_5H_{14}N_2]PdCl_4$ (**2**) were collected at 150 K on a D8 VENTURE Bruker AXS diffractometer and processed with the APEX 3 program suite **[38]**. The used X-ray wavelength was the Mo-Kα radiation (λ=0.71073 Å). Frames integration and data reduction were carried out with the program SAINT **[39]**. The program SADABS **[40]** was employed for multiscan-type absorption corrections. Structures were determined by dual space methods using the SHELXT program **[41]** and refined with full-matrix least-square methods based on F^2 (SHELXL-2014) **[42]** through the WinGX program suite **[43]**. All non-hydrogen atoms were refined with anisotropic atomic displacement parameters. Except Hydrogen atoms linked to Nitrogen atoms that were introduced in the structural model through Fourier difference maps analysis, H atoms were finally included in their calculated positions and treated as riding on their parent atom with constrained thermal parameters. The software Diamond **[44]** was used to create the graphic representations of the crystal structures. Detailed information of the crystallographic data and structures refinements are presented in Table 1. The relevant selected bond lengths and angles are listed in Tables S1-S3.

2.6.Thermal measurements

Thermogravimetric (TG) measurements were performed with a Rigaku Thermoflex instrument under flowing air for $[(R)\text{-}C_5H_{14}N_2]PdCl_4$ (**1**), in the temperature range 300-780K, with a heating rate of 5 °C.min^{-1}. The powdered sample was spread evenly in a large platinum crucible to avoid mass effects. **The differential scanning calorimetry (DSC) analysis of $[(R)\text{-}C_5H_{14}N_2]PdCl_4$ (1) was performed using a PerkinElmer DSC instrument in the temperature ranges between 273 and 625K. The crystalline samples were placed in aluminium crucibles that were heated at scanning rate (5 °C.min^{-1}) under flowing air.**

2.7.Optical and electrical measurements

The optical absorption and reflective spectra of the $[(R)\text{-}C_5H_{14}N_2]PdCl_4$ (**1**) compound were measured at room temperature using a conventional UV–vis absorption spectrometer (Shimadzu, UV-3101PC) in the 200–800 nm wavelength range. Electrical measurements were performed on pellet disks of about 8 mm in diameter and 1mm in thickness in the 10^{-1}to 10^{6} Hz frequency range with a Solartron 1260A impedance analyzer coupled with a dielectric interface in the 323–453K temperature range.

3. Results and Discussion

3.1. X-ray diffraction analysis

Compounds **1** and **2** were obtained as single enantiomers from 2-methylpiperazine in the forms of (R) or [(S)-$C_5H_{12}N_2$]. **The molecule 2-methylpiperazine was selected for this study because this rigid diamine is not likely to exhibit orientational disorder, owing to its low molecular flexibility and multiple points of interaction between each cation and the inorganic components. Meanwhile,** the reactions were focused on the study of the effects of using enantiomorphically pure sources of the chiral forms and Pd(II) ion. Thus, the use of chiral organic amines is one of the best ways for the construction chiral hybrids material that exhibit desirable physical properties **[45-47]**.

The compounds [(R)-$C_5H_{14}N_2$]$PdCl_4$ (**1**) and [(S)-$C_5H_{14}N_2$]$PdCl_4$ (**2**) crystallize in the orthorhombic crystal system with the non-centrosymmetric space group $P2_12_12_1$ (Table 1). The asymmetric unit of each compound consists of a diprotonated (R)/(S)-2-methylpiperazine cation and a tetrachloropalladate anion (Figure 1). The Pd(II) metal center is in a slightly distorted square-planar environment. Indeed, in compound (1), the Pd-Cl bonds range from 2.2977(8) to 2.3105 (8) Å. Similarly, the Pd-Cl bonds in (2) range between 2.2953(8) and 2.3095(8) Å. In (1), the *cis*-Cl-Pd-Cl angles range from 89.43(3) to 90.93(3)°, while the *trans*-Cl-Pd-Cl angles range between 177.96(3) and 179.23(3)°. Likewise, in compound (2), the *cis*-Cl-Pd-Cl angles range between 89.57(3) and 90.80(3)° and between 177.96(4) and 179.25(3)° for the *trans*-Cl-Pd-Cl angles. The selected Pd-Cl bond lengths and the Cl-Pd-Cl bond angles are listed in Table S1.

The analysis of the geometry can be performed using the τ4 metric developed by L. Yang et al. **[48]** for four-coordinated complexes. The τ4 value is calculated as [360°–(α + β)]/141°, where α and β are the two largest angles at the four-coordinated metal atom. A value of zero is indicative of the ideal square-planar geometry, while a value of 1 indicates the ideal tetrahedral geometry. The calculated τ4 parameters for $PdCl_4$ are 0.02 and 0.01 for compounds (1) and (2), respectively. Therefore, the coordination geometry around the Pd(II) ion can be described as a slightly distorted square planar geometry. The geometrical features of $PdCl_4$ entities agree well with those reported for other Pd(II) complexes PdX_4 (X =Cl, Br, I) **[49-51]**.

Within the protonated $[C_5H_{14}N_2]^{2+}$ cations, the C–C and C–N distances and the C–N–C angles range, respectively, from 1.513(4) to 1.529(4) Å, from 1.495(4) to 1.503(4) Å and from 111.2(2) to 112.4(2)° in compound (1). Meanwhile, in compound (2), the C–C bond length varies from 1.513 (5) to 1.522 (5) Å, while the C–N bond length varies from 1.493 (4) to 1.503 (4) Å. The C–N–C angles spreads in the range 111.2 (2) to 112.5 (3)°. The present geometrical characteristics are usually found in other organically templated Pd(II) halides **[52-56]**. The crystal structures of (**1**) and

(**2**) are stabilized by intermolecular hydrogen bonding interactions leading to layers that are parallel to *b* and *c* axes (Figure 2).

The distances of C-H···Cl and N-H···Cl interactions fall in the range of 3.189(3) - 3.803 (3) Å, and the C-H···Cl and N-H···Cl bond angles range from 119(2)° to 164(2)° in compound (**1**). Likewise for compound (**2**), the C-H···Cl and N-H···Cl interactions are in the range of 3.188 (3) - 3.799 (3) Å, and the C-H···Cl and N-H···Cl bond angles range between 119(2)° to 163(1)° in (**2**). The C-H···Cl, N-H···Cl distances and bond angles in (**1**) are slightly changed comparing with those observed in (**2**), by changing of the configuration of organic molecule. These hydrogen bond interactions play a key role in the formation of supramolecular structures. The hydrogen bond parameters are given in Tables S2 and S3.

3.2.Thermal analysis and stabilities

$[(R)\text{-}C_5H_{14}N_2]PdCl_4$ (**1**). **TGA-thermogram of compound (1) reveals two weight loss regions (Figure S4). The first weight loss of 2.7% from 300 to 328K could be attributed to the loss of moisture. The second weight loss in a broad temperature range from 500 to 720 K suggests the decomposition of the organic cation with two chlorine atoms and corresponds to the formation of $PdCl_2$ (observed weight loss, 50.74%, theoretical, 49.34%). It is worth mentioning that the progressive mass loss of 1.8% takes place over the range 725–750K, affording PdO (ICDD 41–1107) as residue [57]. The DSC measurements of $[(R)\text{-}C_5H_{14}N_2]PdCl_4$ (1) show an endothermic peak located at 495K (Figure S5). For this compound, no phase transition can be identified.**

3.3.Optical properties

In order to understand the semiconductor characteristics of $[(R)\text{-}C_5H_{14}N_2]PdCl_4$ (**1**), a study pertaining to the optical properties was undertaken. Figure 3 display the UV-visible absorption spectra at room temperature in 200–800 nm wavelength range and the plots of $(\alpha h\nu)^2$ versus the photon energy ($h\nu$) of $[(R)\text{-}C_5H_{14}N_2]PdCl_4$ (**1**) compound. This spectrum is characterized by a high absorbance in both the ultra-violet and the visible region which means that this compound is a suitable candidate for applications in optoelectronics and photovoltaics **[58-59]**. Three peaks are observed in the UV-visible regions at 243, 309 and 460 nm. **The first peak attributed to the higher energy HOMO-LUMO transition which is a d-d metal-centered transition type involving the promotion of an electron in the d_{yz} orbital to the d_{x2}-$_{y2}$ orbital and indicates the gap energy. The second at 309nm corresponding to the transition of d_{xz} to $d_{x2\ -y2}$, or d_{z2} to $d_{x2\ -y2}$ type. The peak at 460nm indicates the transition between the two both energy levels d_{xy} and d_{x2-y2} [60]**. The band with the maximum absorption in the UV region is produced by electronic transitions from the valence band to the conduction band indicating the gap energy of this material; the other bands correspond to the excitonic transitions **[61]**.

Using absorption values, the coefficient α was calculated and based in the Tauc model **[62]**:

$$(\alpha h\nu)^2=B\ (h\nu-Eg) \qquad (1)$$

where *B* is constant, *Eg* is the optical band gap and *α* is the optical absorption coefficient deduced from the absorbance using the relation:

$$\alpha = \frac{2.303\ A}{d} (\mathbf{2})$$

where *A* is the absorption and *d* the thickness of the samples.

The optical gap energy is determined from the intersection of the extrapolation of the linear part of $(\alpha h\nu)^2$ with the energy axis. The compound $[(R)\text{-}C_5H_{14}N_2)]PdCl_4$ (**1**) has a semiconductor band gap energy (Eg = 3.64 eV) similar to those of $[C_9H_{16}N_2]PdCl_4$ (Eg = 3.26 eV) **[3]** and $[N(C_2H_5)_4]_2Pd_2Cl_6$ (Eg = 4.34 eV) **[60]**. **This difference can be attributed to the symmetry of the chiral cation used in the $[(R)\text{-}C_5H_{14}N_2)]PdCl_4$ (1) compound.**

3.4.Impedance spectroscopy

The impedance spectroscopy was used to differentiate between the grain and grain boundary response by attributing the observed relaxations and determining the equivalent circuit. **Figure 4** shows the Nyquist plots at different temperatures. The radius of these semicircle decreases with increasing temperature indicating a semiconductor character of this material which confirms the optical result **[63]**. **Except at 383K, the radius of the semicircle at law frequencies corresponding to the grain boundaries increases which indicates the release of H_2O absorbed by this material.** Two semi-circles associated to the grain and grain boundaries are observed in these spectra at higher and lower frequencies, respectively. The centers of all semi-circles are shifted down to the real axis indicating a non-Debye type relaxation process and confirms that the complex impedance curves of this compound obey the Cole–Cole formalism. The equivalent circuit which ensures minimum error and good confirmation between the theoretical and experimental curve shows two cells in series where the first one is formed by a resistor (R), a capacitor (C) and a fractal capacitor (CPE) mounted in parallel and the seconde one is formed by a parallel combination of resistor R with a capacitor CPE **(Figure 5)**.

The impedance of the constant phase element CPE [64] is normally used to represent the deviation from Debye's model and thus the distribution of relaxation times approach is given by

$$Z_{CPE} = \frac{1}{Q(j\omega)^{\alpha}} \qquad \mathbf{(3)}$$

where Q is the capacitance value of the CPE impedance and (0 ≤α≤1) relates to the deviation degree with respect to the pure capacitor value. This simulation allows to separate between the resistances of the grain and grain boundaries. The parameters values extracted from the equivalent circuit using Z-view software allow to identify the conductivities of the grain at each temperature from the following expression **[65]**:

$$\boldsymbol{\sigma_g = e/R_g*S} \qquad \textbf{(4)}$$

where e/S (cm^{-1}) represents the sample geometrical ratio.

The temperature dependence of Rg is given in **figure 6**. This variation is described by the Arrhenius law. The calculated activation energy value is equal to E_g = 0.71 eV.

3.5.Complexes modulus analysis

Figures 7 display the imaginary part of modulus spectra as function of frequencies at different temperature. **At low frequencies, M" exhibited very small values and tended to zero suggesting the suppression of the electrode polarization effect**. Two relaxations are observed corresponding to the grain at high frequency and to the grain boundaries at low frequency. These peaks shift to higher frequencies when the temperature increases evidence an ionic conduction character of this sample. **Except, the relaxation in the curve at 383K where this material shows a disturbance due to the release of H_2O. The low frequency side of the peak indicates the range of frequencies in which ions can successfully jump from one site to the neighboring site. The high frequencies of the peak M″ represent the frequency range in which the ions are spatially confined to their potential wells and can make a localized motion in the well [66]. The region where the peak occurs indicates the transition of a long-range mobility to short-range mobility with increasing frequency.**

The adjustment function of Kohlrausch–Williams–Watts (KWW) allows a direct analysis of the M" variation versus frequency which was modified by Bergman **[67]**. The imaginary part of the M"(ω) has been given according to the following relationship **[67-68]**:

$$\begin{aligned} M'' = M''_{1max} / ((1-\beta_1) + (\beta_1/1+\beta_1))[(\omega_{1max}/\omega + (\omega/\omega_{1max})\beta_1] + \\ [M''_{2max} / ((1-\beta_2) + (\beta_2/1+\beta_2) + (\beta_2/1+\beta_2))[(\omega_{2max}/\omega) + (\omega/\omega_{2max})\beta_2] \end{aligned} \qquad \textbf{(5)}$$

$\omega_{max=}$ 2*π*$f_{max,}$ where f_{max} is the frequency corresponding to the relaxation of modulus M", β (between 0 and 1) indicates the degree of deviation from the Debye-type relaxation. The fitted spectra of M" based on the equation (5) is in good agreement with the experimental data. The plot of ln (ω_{max}), corresponding to the maximum of the M" of the grain, as function 1000/T obeys the

Arrhenius law **(Figure 8)** and the activation energy value is equal to E_g = 0.69 eV **which is near to the energy determined by the conductivity of grain.**

3.6.AC electrical conductivity

The conduction mechanism within the synthesized material is complicated. According to Elliot theory **[69]**, we can attribute this mechanism either to hopping of charge carriers or to Tunnel effect. This attribution is related to the variation of the parameter (S), the exponent in the Jonscher's law **[70]**, which reflects the interaction between the moving load and its environment **[71]**. In this context, we have plotted the variation of the AC conductivity as a function of frequency at different temperatures (Figure 9). This variation is described by Jonscher's law and shows two regions: (i) a frequency-independent plateau and (ii) high-frequency dispersion. **The conduction electrons at low frequency are more active at grain boundaries, but high frequency grains are more contributing for increasing the electrical conductivity for which grain boundaries need more energy for electrical conduction at low frequency, as they possess high resistance.** The simulation of these spectra and the good conformity between the experimental and theoretical spectra makes it possible to deduce the values of the exponent (S) and the DC conductivity. Figure 10 shows the variation of the DC conductivity as function of temperature which is described by the Arrhenius law and confirms the σ_g and ω_{max} variations. The calculated activation energy is equal to 0.43 eV which is different to those found in the σ_g and ω_{max} variation. This result indicates that the conduction is not described solely by the hopping mechanism. To cheek the conduction behavior of this material, based on the Elliot theory **[69]**, the variation of the exponent (S) reported in figure 11 shows a decrease of S as a function of temperature up to a minimum then it's increase. This behavior, **based in the Elliot theory**, indicates that the overlapping large polaron tunneling (OLPT) is the most suitable model to describe the conduction mechanism in this material **[69]**.

4. Conclusion

In conclusion, a pair of enantiomorphic organic–inorganic hybrid palladium halides, [(R)-$C_5H_{14}N_2$]$PdCl_4$ (**1**) and [(S)-$C_5H_{14}N_2$]$PdCl_4$ (**2**), were successfully obtained with the templating of chiral amines and both of them are lucky to crystallize in the chiral space group $P2_12_12_1$. The geometry of the $[PdCl_4]^{2-}$ anions is square planar around the metal ions in both compounds. The crystal packing of the compounds is stabilized by intermolecular hydrogen bonds giving rise to a supramolecular architecture. Besides, compound (**1**) exhibits a band gap of 3.64 eV. The semiconductor character of this material is identified by the optical, electrical studies, the equivalent circuit and the conduction mechanism. This work underlines the importance of palladium halides as a new kind of chiral semiconducting materials.

Appendix

CCDC 2196155 - 2196156 contain the supplementary crystallographic data for this paper. The data can be obtained free of charge from The Cambridge Crystallographic Data Centre via www.ccdc.cam.ac.uk/structures.

Acknowledgments

The authors thank the University of Sfax-Tunisia for financial support and CDIFX (UMR 6226, Univ. Rennes 1) for X-ray diffraction data collection.

Conflicts of interest

There are no conflicts to declare.

References

[1] (a) A. Kojima, K. Teshima, Y. Shirai, T. Miyasaka, J. Am. Chem. Soc., 2009, **131**, 6050; (b) C. C. Stoumpos, M. G. Kanatzidis, Adv. Mater., 2016, **28**, 5778; (c) J. Burschka, N. Pellet, S.-J. Moon, R. Humphry-Baker, P. Gao, M. K. Nazeeruddin, M. Graetzel, Nature, 2013, **499**, 316; (d) J. Yu, J. Zheng, N. Tian, L. Li, Y. Qu, Y. Huang, Y. Luo, W. Tan, **RSC Adv.**, 2022, **12**, 23578; (e) P. Basumatary, P. Agarwal, Mater. Res. Bull., 2021, **149**, 111700; (f) J. Liu, X. Zheng, O. F. Mohammed, O. M. Bakr, Acc. Chem. Res. 2022, **55**, 262; (g) T. J. Huang, Z. X. Thiang, X. Yin, C. Tang, G. Qi, H. Gong, Chem. Eur. J. 2016, **22**, 2146.

[2] (a) M. Li, J. Zhou, G. Zhou, M. S. Molokeev, J. Zhao, V. Morad, M. V. Kovalenko, Z. Xia, Angew. Chem. Int. Ed., 2019, **58**, 18670; (b) Y. Dong, Y. Han, R. Chen, Y. Lin, B.-B. Cui, J. Lumin., 2022, **249**, 119013.

[3] (a) J. Choi, J. S. Han, K. Hong, S. Y. Kim, H. W. Jang, Adv. Mater., 2018, **30**, 1704002 ; (b) H. Bouznif, F. Hajlaoui, K. Karoui, N. Audebrand, M. Cordier, T. Roisnel, N. Zouari, J. Solid State Chem., 2022, **311**, 123149.

[4] L. N. Quan, F. P. G. de Arquer, R. P. Sabatini, E. H. Sargent, Adv. Mater., 2018, **30**, 1801996.

[5] (a) B. Saparov, D. B. Mitzi, Chem. Rev., 2016, **116**, 4558; (b) Z. Yi, N. H. Ladi, X. Shai, H. Li, Y. Shen, M. Wang, Nanoscale Adv., 2019, **1**, 1276.

[6] B. Sun, X. F. Liu, X. Y. Li, Y. Cao, Z. Yan, L. Fu, N. J. Tang, Q. Wang, X. F. Shao, D. Z. Yang, H. L. Zhang, Angew. Chem., Int. Ed., 2020, **59**, 203.

[7] (a) T. Sakami, T. Ohtani, Y. Matsumoto, D. Ochi, X. Xi, S. Kamikawa, J. Ohyama, I. Ishii, T. Suzuki, Solid State Commun., 2019, **290**, 49; (b) Z. Hu, H. Zhao, Z. Cheng, J. Ding, H. Gao, Y. Han, S. Wang, Z. Xu, Y. Zhou, T. Jia, H. Kimura, M. Osada, Phys. Chem. Chem. Phys., 2020, **22**, 4235; (c) S. Deswal, S. K. Singh, P. Rambabu, P. Kulkarni, G. Vaitheeswaran, B. Praveenkumar, S. Ogale, R. Boomishankar, Chem. Mater., 2019, **31**, 4545.

[8] (a) K.-Z. Du, Q. Tu, X. Zhang, Q. Han, J. Liu, S. Zauscher, D. B. Mitzi, Inorg. Chem., 2017, **56**, 9291; (b) H. Chen, H. Wang, J. Wu, F. Wang, T. Zhang, Y. Wang, D. Liu, S. Li, R. V. Penty, I. H. White, Nano Res., 2020, **13**, 1997.

[9] E. Yablonovitch, Science, 2016, **351**, 1401.

[10] C. Katan, N. Mercier, J. Even, Chem. Rev., 2019, **119**, 3140.

[11] (a) S. Han, X. Liu, Y. Liu, Z. Xu, Y. Li, M. Hong, J. Luo and Z. Sun, J. Am. Chem. Soc., 2019, **141**, 12470; (b) S. Ahmad, X. Guo, Chin. Chem. Lett., 2018, **29**, 657.

[12] W. Ke, C. C. Stoumpos, M. G. Kanatzidis, Adv. Mater., 2019, **31**, 1803230.

[13] (a) M. Li, J. Zhou, G. Zhou, M. S. Molokeev, J. Zhao, V. Morad, M. V. Kovalenko, Z. Xia, Angew. Chem. Int. Ed., 2019, **131**, 18843; (b) M. Li, J. Zhou, M. S. Molokeev, X. Jiang, Z. Lin, J. Zhao, Z. Xia, Inorg. Chem., 2019, **58**, 13464.

[14] D. Cortecchia, H. A. Dewi, J. Yin, A. Bruno, S. Chen, T. Baikie, P. P. Boix, M. Grätzel, S. Mhaisalkar, C. Soci, N. Mathews, Inorg. Chem., 2016, **55**, 1044.

[15] Z. Ma, L. Wang, X. Ji, X. Chen, Z. Shi, J. Phys. Chem. Lett., 2020, **11**, 5517.

[16] (a) H. Zhou, X. Cui, C. Yuan, J. Cui, J. Cu, S. Shi, G. He, Y. Wang, J. Wei, X. Pu, W. Li, D. Zhang, J. Wang, X. Ren, H. Ma, X. Shao, X. Wei, J. Zhao, X. Zhang, J. Yin, ACS Omega, 2018, **3**, 13960.

[17] C. Zhou, Y. Chu, Y. Zhong, C. Wang, Y. Liu, H. Zhang, B. Wang, X. Feng, X. Yu, X. Zhang, Y. Sun, X. Li, G. Zhao, Phys. Chem. Chem. Phys., 2020, **22**, 17299.

[18] G. Long, R. Sabatini, M. I. Saidaminov, G. Lakhwani, A. Rasmita, X. Liu, E. H. Sargent, W. Gao, Nat. Rev. Mater., 2020, **5**, 423.

[19] V. Y. Sirenko, O. I. Kucheriv, D. D. Naumova, I. V. Fesych, R. P. Linnik, I.-A. Dascălu, S. Shova, I. O. Fritsky, I. A. Gural'skiy, New J. Chem., 2021,**45**, 12606.

[20] B. Ni, H. Cölfen, SmartMat., 2021, **2**,17.

[21] M. Ben Haj Salah, N. Mercier, M. Allain, N. Zouari, C. Botta, J. Mater. Chem. C, 2019, **7**, 4424.

[22] M. W. Heindl, T. Kodalle, N. Fehn, L. K. Reb, S. Liu, C. Harder, M. Abdelsamie, L. Eyre, I. D. Sharp, S. V. Roth, P. Müller-Buschbaum, A. Kartouzian, C. M. Sutter-Fella, F. Deschle, Adv. Optical Mater., 2022, **10**, 2200204.

[23] Y. Peng, Y. Yao, L. Li, X. Liu, X. Zhang, Z. Wu, S. Wang, C. Ji, W. Zhang, J. Luo, Chem. Asian J., 2019, **14**, 2273.

[24] F. Ge, B.-H. Li, P. Cheng, G. Li, Z. Ren, J. Xu, X.-H. Bu, Angew. Chem. Int. Ed., 2022, **134**, 202115024.

[25] S. Qi, F. Ge, X. Han, P. Cheng, R. Shi, C. Liu, Y. Zheng, M. Xin, J. Xu, Dalton Trans., 2022,**51**, 8593.

[26] H.-Y. Zhang, Y.-Y. Tang, P.-P. Shi, R.-G. Xiong, Acc. Chem. Res., 2019, **52**, 1928.

[27] L.-S. Li, Y.-H. Tan, W.-J. Wei, H.-Q. Gao, Y.-Z. Tang**,** X.-B. Han, ACS Appl. Mater. Interfaces, 2021, **13**, 2044.

[28] S. Ma, J. Ahn, J. Moon, Adv. Mater., 2021, **33**, 2005760.

[29] Y. Lu, Q. Wang, R. He, F. Zhou, X. Yang, D. Wang, H. Cao, W. He, F. Pan, Z. Yang, C. Song, Angew. Chem. Int. Ed., 2021, **60**, 23578.

[30] (a) D. G. Billing, A. Lemmerer, CrystEngComm, 2006, **8**, 686; (b) Billing, D. G. Lemmerer, Acta Cryst. E, 2003, **59**, 381; **(c) T. Sheikh, S. Maqbool, P. K. Rajput, P. Mandal, A. Nag, Chem. Commun., 2022, 58, 7650**; **(d) P. K. Rajput, A. K. Poonia, S. Mukherjee, T. Sheikh, M. Shrivastava, K. V. Adarsh, A. Nag, J. Phys. Chem. C 2022, 126, 9889**.

[31] Y. Peng, Y. Yao, L. Li, Z. Wu, S. Wang, J. Luo, J. Mater. Chem. C, 2018, **6**, 6033.

[32] (a) L-L. Zhu, Y-E. Huang, Y-P. Lin, X-Y. Huang, H-Q. Liu, D.B. Mitzi, K-Z. Du, Polyhedron, 2019, **158**, 445; **(b) M. K. Jana, R. Song, H. Liu, D. Raj Khanal, S. M. Janke, R. Zhao, C. Liu, Z. V. Vardeny, V. Blum, D. B. Mitzi, Nat. Commun., 2020, 11, 4699.**

[33] C.-K. Yang, W.-N. Chen, Y.-T. Ding, J. Wang, Y. Rao, W.-Q. Liao,Y.-Y. Tang, P.-F. Li, Z.-X. Wang, R.-G. Xiong, Adv. Mater., 2019, **31**, 1808088.

[34] R.-G. Xiong, S.-Q. Lu, Z.-X. Zhang, H. Cheng, P.-F. Li, W.-Q. Liao, Angew. Chem., Int. Ed., 2020, **59**, 9574.

[35] P. Gonzalez-Izquierdo, O. Fabelo, L. Canadillas-Delgado, G. Beobide, O. Vallcorba, J. Salgado-Beceiro, M. Sanchez-Andujar, C. Martin, J. Ruiz-Fuentes, J. E. Garcia, M. T. Fernandez-Diaz, I. de Pedro, J. Mater. Chem. C, 2021, **9**, 4453.

[36] (a) F. Hajlaoui, H. Naïli, S. Yahyaoui, A. J. Norquist, T. Mhiri, T. Bataille, J. Organomet. Chem., 2012, **700**, 110; (b) J. H. Olshansky, T. T. Tran, K. J. Hernandez, M. Zeller, P. S. Halasyamani, J. Schrier, A. J. Norquist, Inorg. Chem., 2012, **51**, 11040; (c) T. R. Veltman, A. K. Stover, A. N. Sarjeant, K. M. Ok, P. S. Halasyamani, A. J. Norquist, Inorg. Chem., 2006, **45**, 5529.

[37] (a) S. J. Choyke, S. M. Blau, A. A. Larner, A. N. Sarjeant, J. Yeon, P. S. Halasyamani, A. J. Norquist, Inorg. Chem., 2009, **48**, 11277; (b) E. A. Muller, R. J. Cannon, A. N. Sarjeant, K. M. Ok, P. S. Halasyamani, A. J. Norquist, Cryst. Growth Des., 2005, **5**, 1913; (c) X. Jia, Y. Zheng, P. Cheng, X. Han, L. Xu, J. Xu, **Dalton Trans.**, 2022,**51**, 7248.

[38] APEX3 program suite V2016.1–0, Bruker AXS Inc., Wisconsin, USA.

[39] G. M. Sheldrick, SAINT Version 8.37A, Bruker AXS Inc., Wisconsin, USA 2013.

[40] G. M. Sheldrick, SADABS version 2014/5, SADABS Bruker AXS Inc., Madison, Wisconsin, USA.

[41] G. Sheldrick, *ActaCrystallogr., A* 2015, **71**, 3.

[42] G. Sheldrick,*ActaCrystallogr., C* 2015, **71**, 561.

[43] L. Farrugia, *J. Appl. Crystallogr.*,2012, **45**, 849.

[44] K. Brandenburg, M. Berndt, Diamond (version 2), Crystal Impact, Bonn, 2001.

[45] Y. Wu, H. Jiang, S. Jiao, D. Li, Z. Gao, B. Niu, D. Wu, S. Chen, H.-L. Cai, X. Wu, Adv. Optical Mater., 2022, **10**, 2101905.

[46] J. Ahn, E. Lee, J. Tan, W. Yang, B. Kim, J. Moon, Mater. Horiz., 2017, **4**, 851.

[47] P. K. Rajput, A. K. Poonia, S. Mukherjee, T. Sheikh, M. Shrivastava, K. V. Adarsh, A. Nag, J. Phys. Chem. C, 2022, **126**, 9889.

[48] L. Yang, D. R. Powell, R. P. Houser. Dalton Trans., 2007, **9**, 955.

[49] R. Wysokinski, W. Zierkiewicz, M. Michalczyk, T. Maris, S. Scheiner, Molecules, 2022, **27**, 2144.

[50] I.A. Efimenko, A.V. Churakov, N.A. Ivanova, O.S. Erofeeva, L.I. Demina, Russ. J. Inorg. Chem., 2017, **62**, 1469.

[51] W. Zierkiewicz, M. Michalczyk, T. Maris, R. Wysokiński, S. Scheiner, Chem. Commun., 2021,**57**, 13305.

[52] J. M. Chitanda, J. W. Quail, S. R. Foley, Acta Cryst., 2008, **64**, 907.

[53] F. Neve, A. Crispini, CrystEngComm., 2003, **5**, 265.

[54] A. Naghipour, A. Ghorbani-Choghamarani, F. Heidarizadi, B. Notash, Polyhedron, 2016, **105**, 18.

[55] X. Liu, N. Zhang, B. Tang, M. Li, Y.-W. Zhang, Z. G. Yu,H. Gong, J. Phys. Chem. Lett., 2018, **9**, 5862.

[56] X. Liu, T. J. Huang, L. Zhang, B. Tang, N. Zhang, D. Shi, H. Gong, Chem. Eur. J., 2018, **24**, 4991.

[57] International Center of Diffraction Data. Powder diffraction file: release, New Square. 1996, PDF no. 41–1107.

[58] V. Priyanka, A. S. VijaiAnand, K. Mahesh and S. Karpagam, IOP Conf. Ser.: Mater. Sci. Eng., 2017, **263**, 022016.

[59] R. Kalthoum, M. Ben Bechir, A. Ben Rhaiem, Physica E Low Dimens. Syst. Nanostruct., 2020, **124**, 114235.

[60] I. Dakhlaoui, K. Karoui, F. Hajlaoui, F. Jomni, Appl. Organomet. Chem., 2020, **34**, 5990.

[61] P. Makuła, M. Pacia, W. Macyk, J. Phys. Chem. Lett., 2018, **9**, 6814.

[62] K. Trabelsi, K. Karoui, F. Jomni, A. Ben Rhaiem, J. Alloys Compd., 2021, **867**, 159099.

[63] K. Karoui, F. Hajlaoui, N. Audebrand, T. Roisnel, A. Ben Rhaiem, J. Alloys Compd., 2020, **844**, 156115.

[64] J. R. Macdonald, Impedance spectroscopy. Emphasizing solid materials and systems, J. Wiley and Sons, 1987, 346.

[65] L. Mathes, T. Gigl, M. Leitner, C. Hugenschmidt, Phys. Rev. B, 2020, **101**, 134105.

[66] K.P. Padmasree, D.K. Kanchan, A.R. Kulkarni, Solid State Ionics, 2006, 177, 475.

[67] R. Bergman, J. Appl. Phys., 2000, **88**, 1356.

[68] M . D. Migahed, N. A. Bakr, M. I. Abdel-Hamid, O. El-Hanafy, M. El-Nimr, J. Appl. Polym. Sci., 1996, **59**, 655.

[69] S. R. Eliott, J. Adv. Phys., 1987, **36**, 135.

[70] A. K. Jonscher, Nature 1977, **267**, 673.

[71] N. F. Mott, E. A. Davis, Oxford. 1972, **12**, 55.

Figure captions

Figure 1: The photograph of [(R)-$C_5H_{14}N_2$]$PdCl_4$ (1) **(a)** and [(S)-$C_5H_{14}N_2$]$PdCl_4$ (2) **(c).** Asymmetric units of [(R)-$C_5H_{14}N_2$]$PdCl_4$ (1) **(b)** and [(S)-$C_5H_{14}N_2$]$PdCl_4$ (2) **(d)**. Hydrogen bonds are shown with red dotted lines.

Figure 2(a): The packing diagram of [(R)-$C_5H_{14}N_2$]$PdCl_4$ (1). The dashed lines stand for the hydrogen bonds.

Figure 2(b): The packing diagram of [(S)-$C_5H_{14}N_2$]$PdCl_4$ (2). The dashed lines stand for the hydrogen bonds.

Figure 3: The UV-visible absorbance spectrum and the Tauc plot of the [(R)-$C_5H_{14}N_2$]$PdCl_4$ (1).

Figure 4: **The Nyquist diagram and equivalent circuit at several temperature of [(R)-$C_5H_{14}N_2$]$PdCl_4$ (1).**

Figure 5: **Example of experimental and simulated curve of impedance diagram at 343K and 403K of [(R)-$C_5H_{14}N_2$]$PdCl_4$ (1).**

Figure 6: Variation of the σ_g versus 1000/T of the [(R)-$C_5H_{14}N_2$]$PdCl_4$ (1) compound.

Figure 7: Variation of the imaginary part of Modulus versus frequencies of [(R)-$C_5H_{14}N_2$]$PdCl_4$ (1).

Figure 8: Variation of the ω_{max} versus 1000/T of [(R)-$C_5H_{14}N_2$]$PdCl_4$ (1).

Figure 9: Experimental and simulations of the AC conductivity versus frequencies of the [(R)-$C_5H_{14}N_2$]$PdCl_4$ (1).

Figure 10: Variation of the σ_{dc} versus 1000/T of [(R)-$C_5H_{14}N_2$]$PdCl_4$ (1).

Figure 11: Variation of the exponent (S) versus temperature of [(R)-$C_5H_{14}N_2$]$PdCl_4$ (1).

Table 1. Crystallographic data for [(R)/(S)-$C_5H_{14}N_2$]$PdCl_4$ compounds.

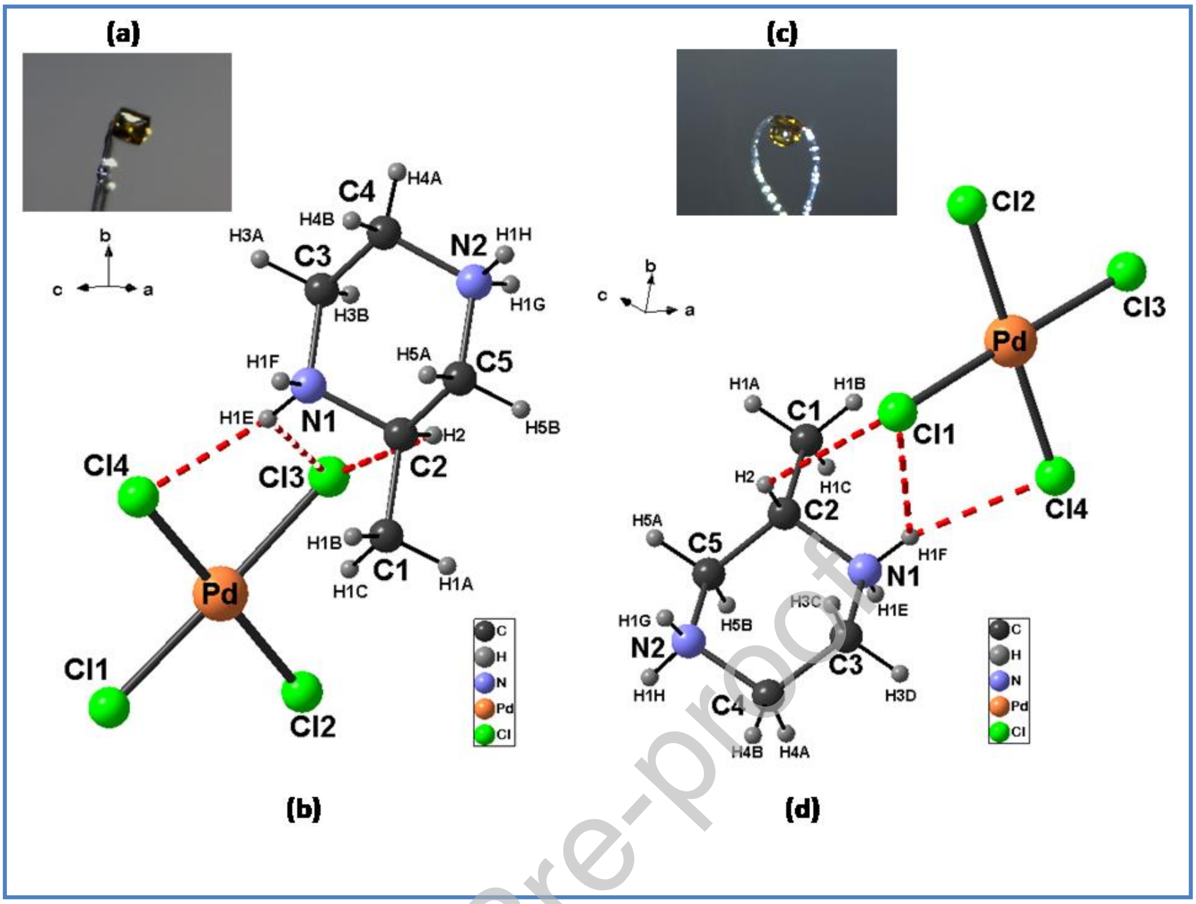

Figure 1: The photograph of $[(R)\text{-}C_5H_{14}N_2]PdCl_4$ (1) **(a)** and $[(S)\text{-}C_5H_{14}N_2]PdCl_4$ (2) **(c).** Asymmetric units of $[(R)\text{-}C_5H_{14}N_2]PdCl_4$ (1) **(b)** and $[(S)\text{-}C_5H_{14}N_2]PdCl_4$ (2) **(d)**. Hydrogen bonds are shown with red dotted lines.

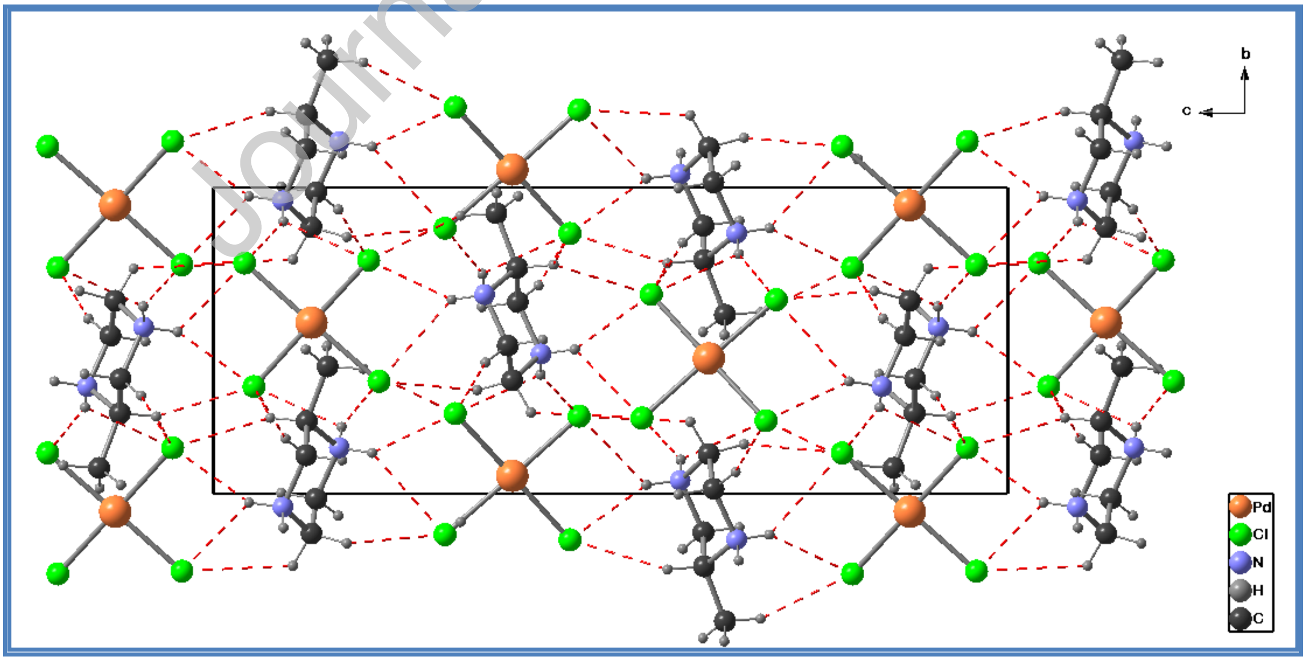

Figure 2(a): The packing diagram of $[(R)\text{-}C_5H_{14}N_2]PdCl_4$ (**1**), projected along the *a*-axis. The red dashed lines stand for the hydrogen bonds.

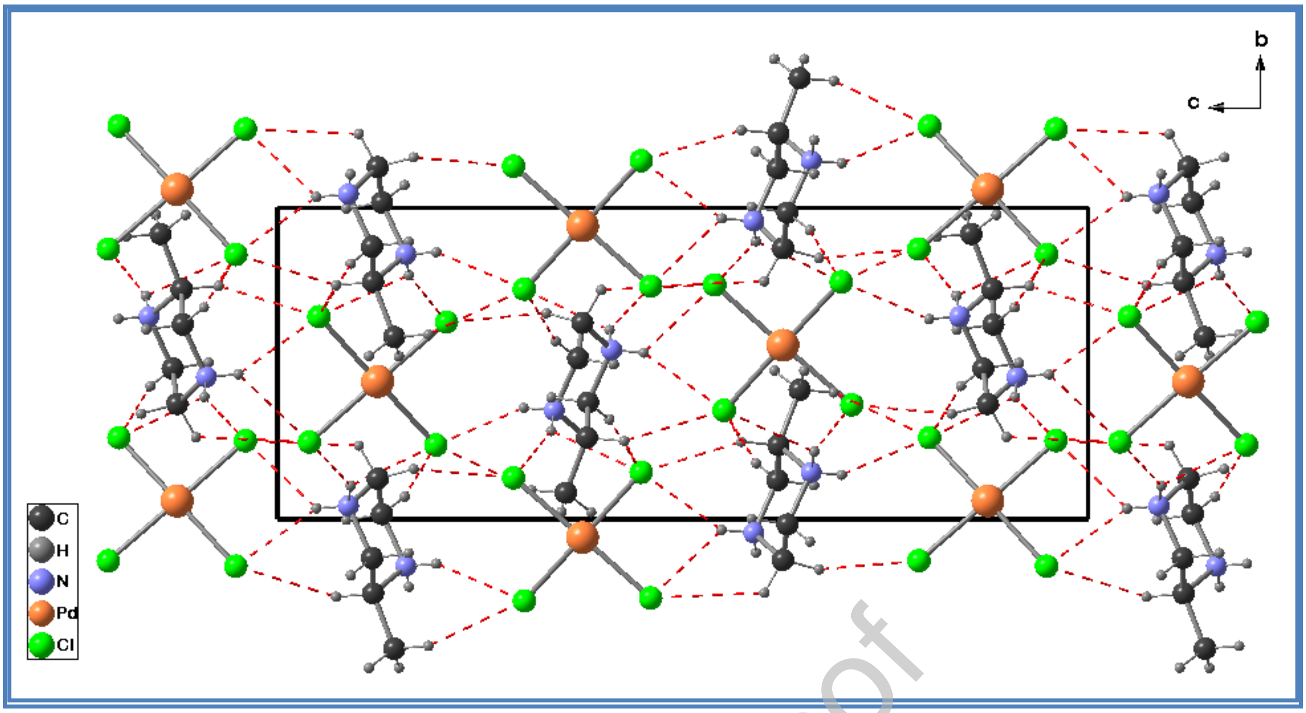

Figure 2(b): The packing diagram of [(S)-$C_5H_{14}N_2$]$PdCl_4$ (**2**), projected along the *a*-axis. The red dashed lines stand for the hydrogen bonds.

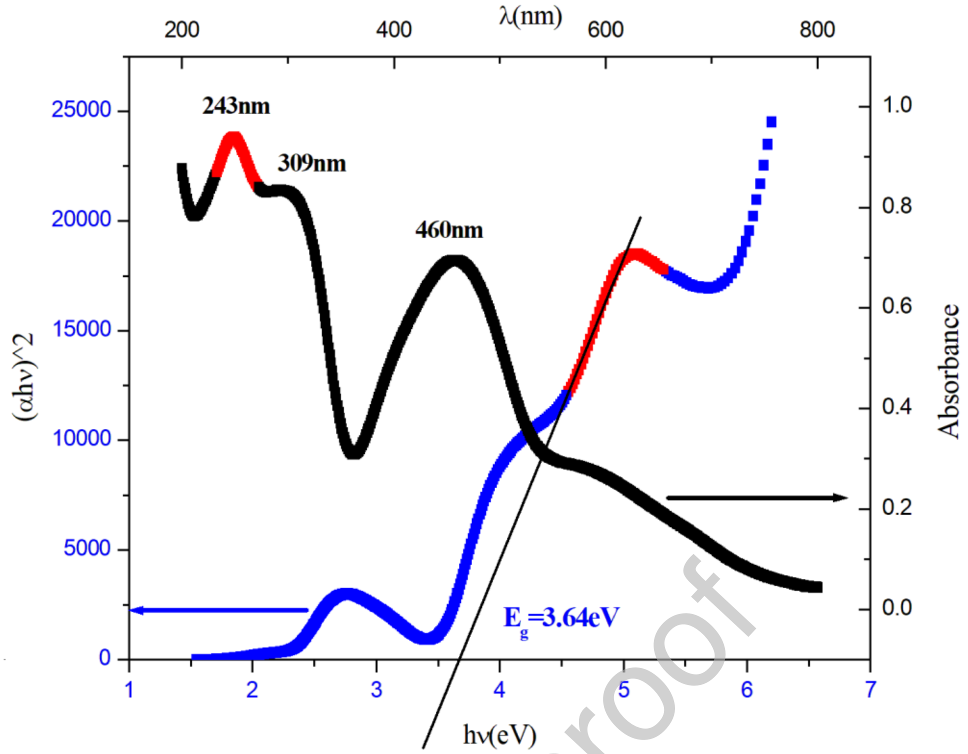

Figure 3: The UV-visible absorbance spectrum **(black)** and the Tauc plot **(blue)** of the [(R)-$C_5H_{14}N_2$]$PdCl_4$ (**1**).

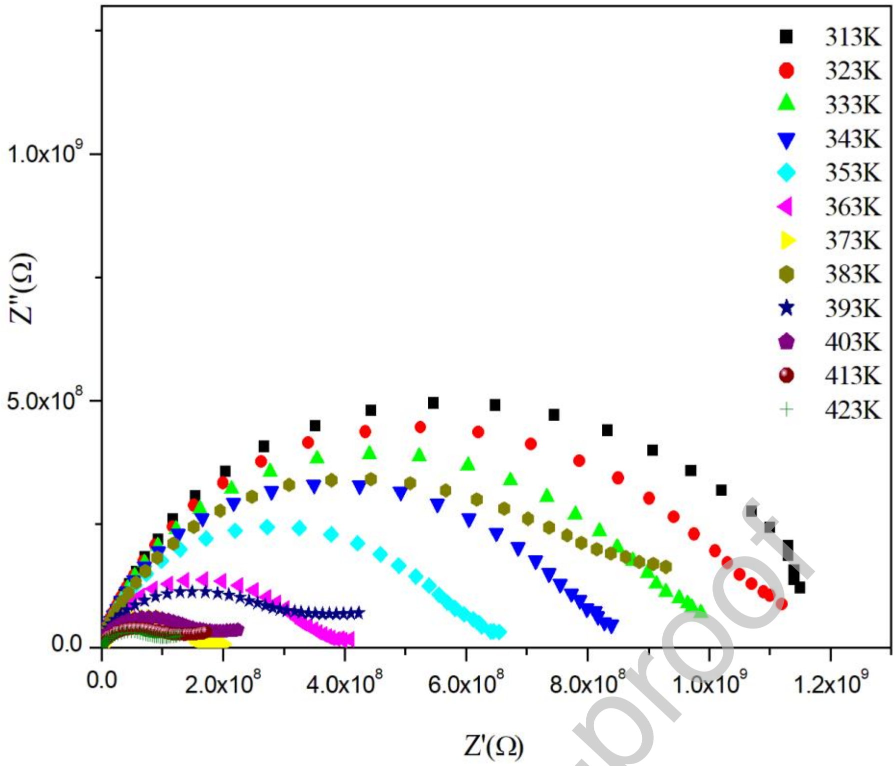

Figure 4: The Nyquist diagram and equivalent circuit at several temperature of [(R)-$C_5H_{14}N_2$]$PdCl_4$ (**1**).

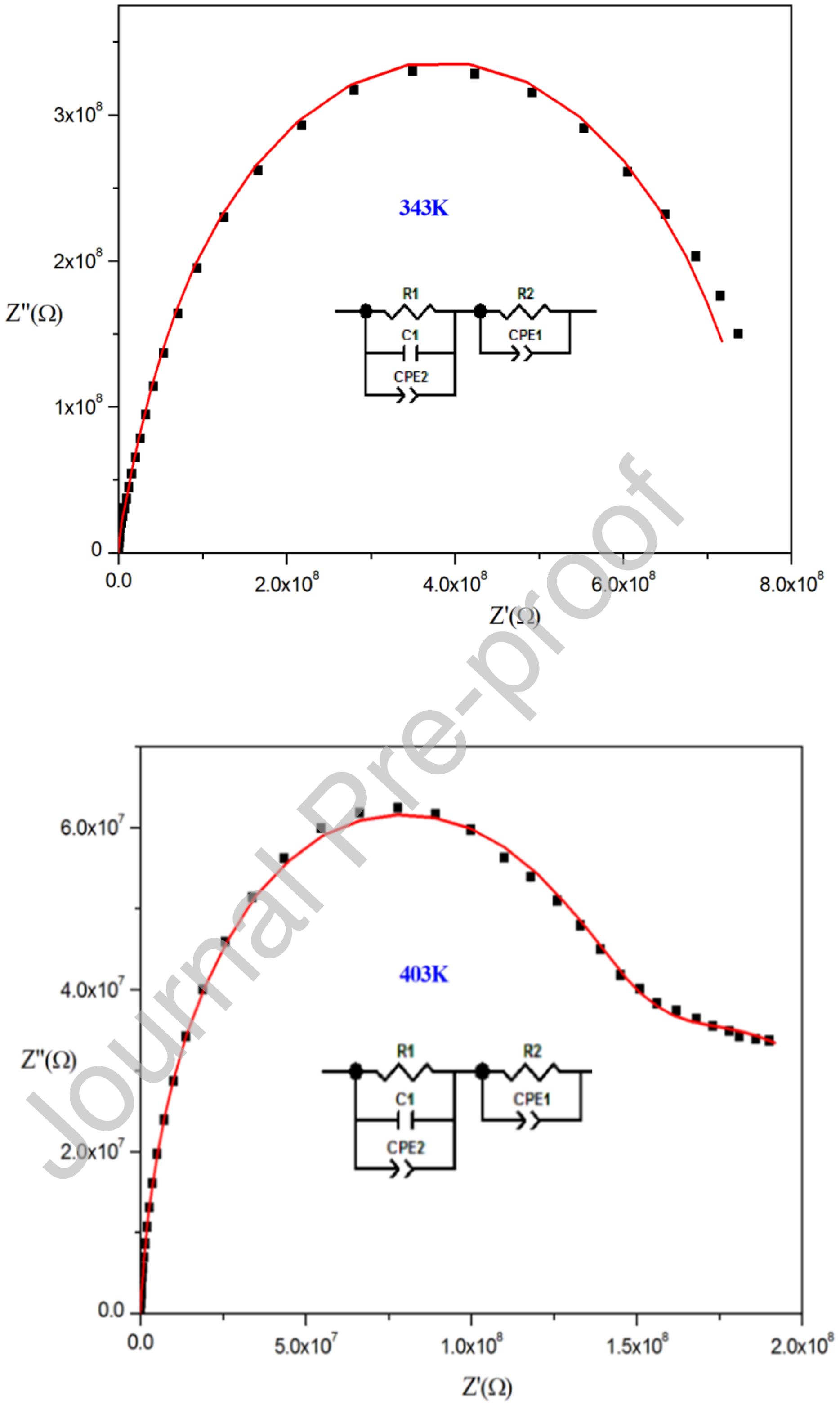

Figure 5: Example of experimental and simulated curve of impedance diagram at 343K and 403K of [(R)-$C_5H_{14}N_2$]$PdCl_4$ (1).

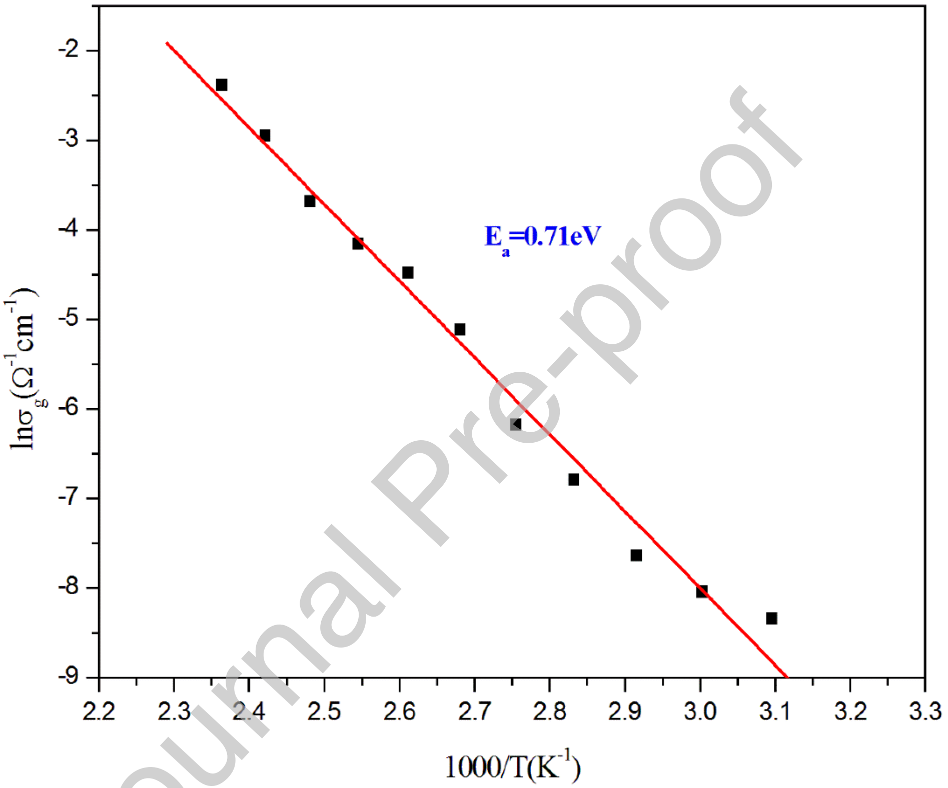

Figure 6: Variation of the σ_g versus 1000/T of the [(R)-$C_5H_{14}N_2$]$PdCl_4$ (**1**) compound.

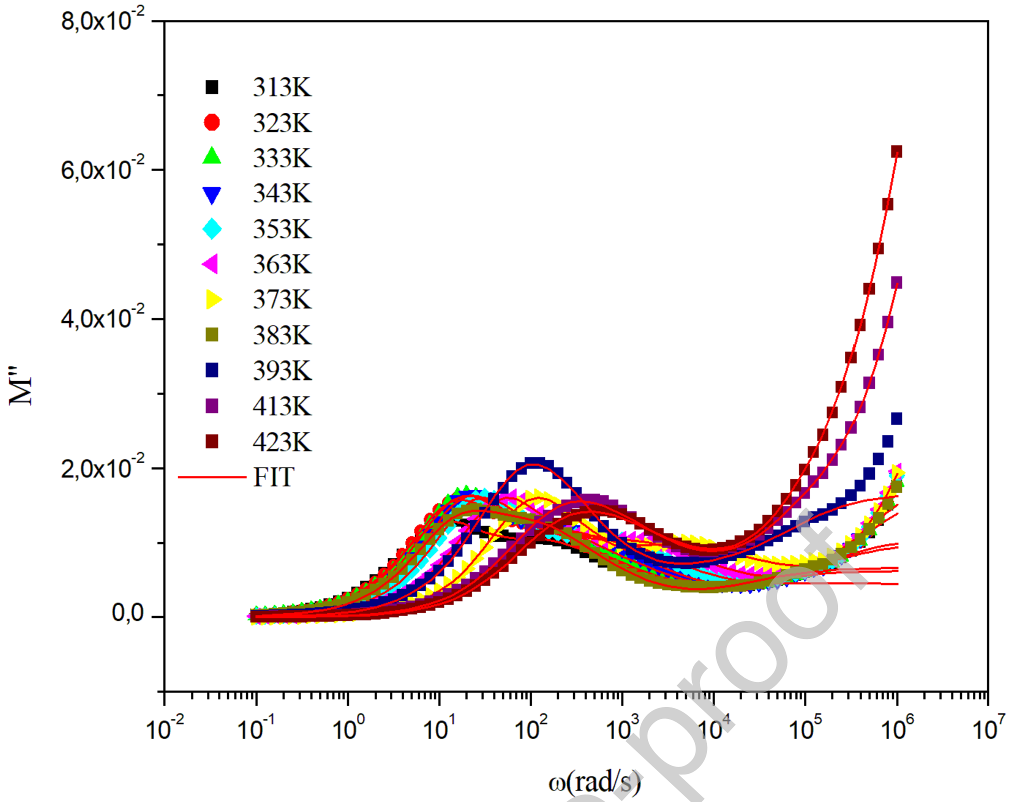

Figure 7: Variation of the imaginary part of Modulus versus frequencies of [(R)-$C_5H_{14}N_2$]$PdCl_4$ (1).

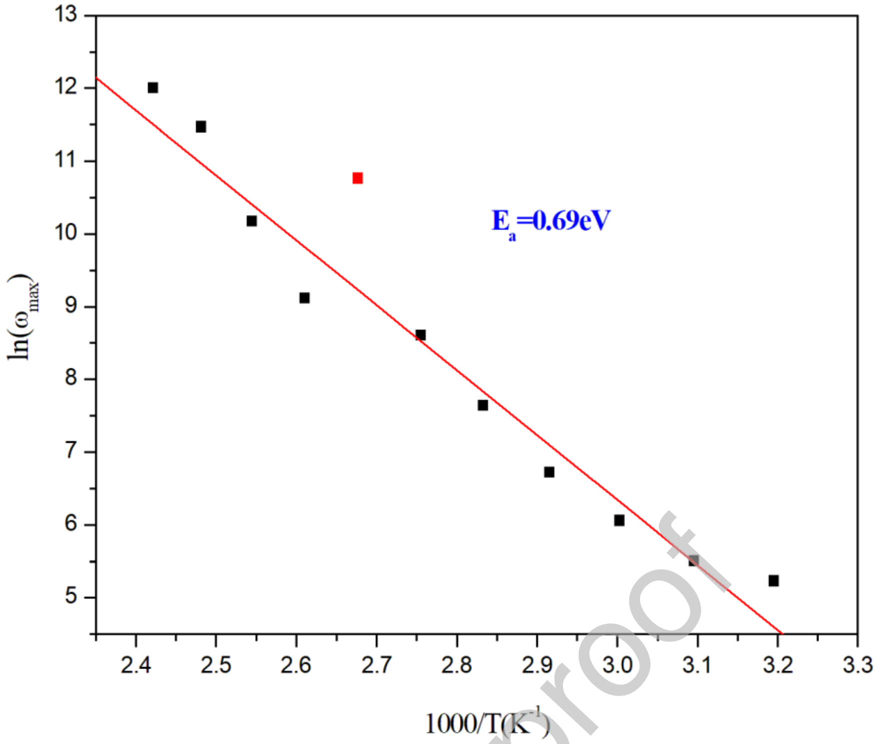

Figure 8: Variation of the ω_{max} versus 1000/T of [(R)-$C_5H_{14}N_2$]$PdCl_4$ (1).

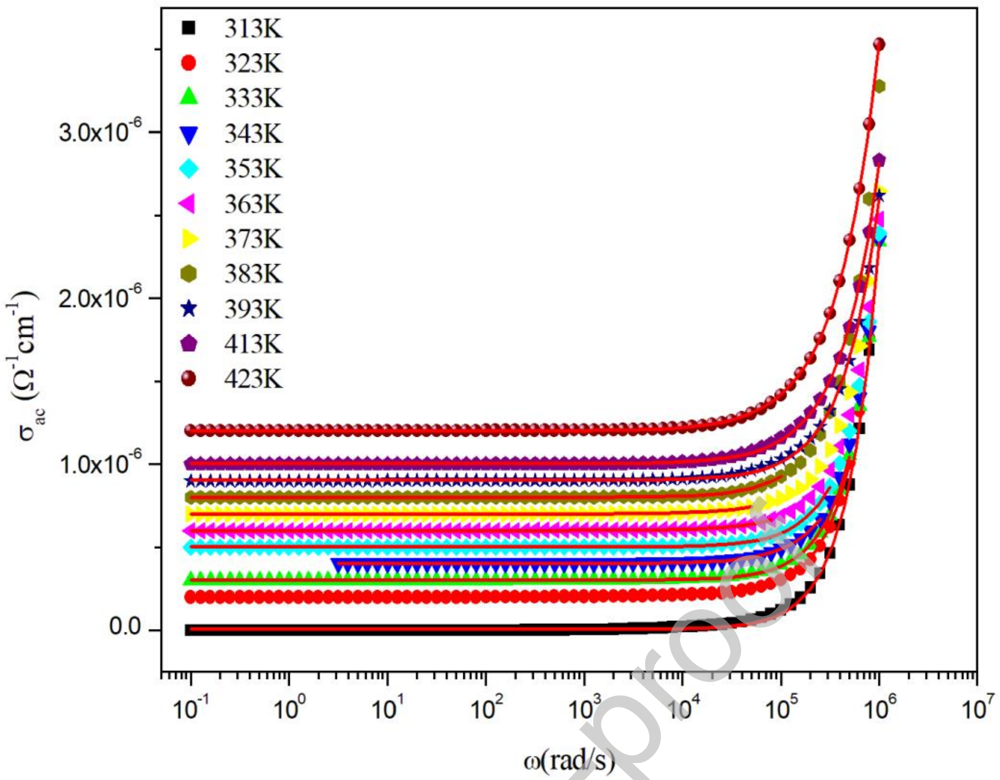

Figure 9: Experimental and simulations of the AC conductivity versus frequencies of the [(R)-$C_5H_{14}N_2$]$PdCl_4$ (1).

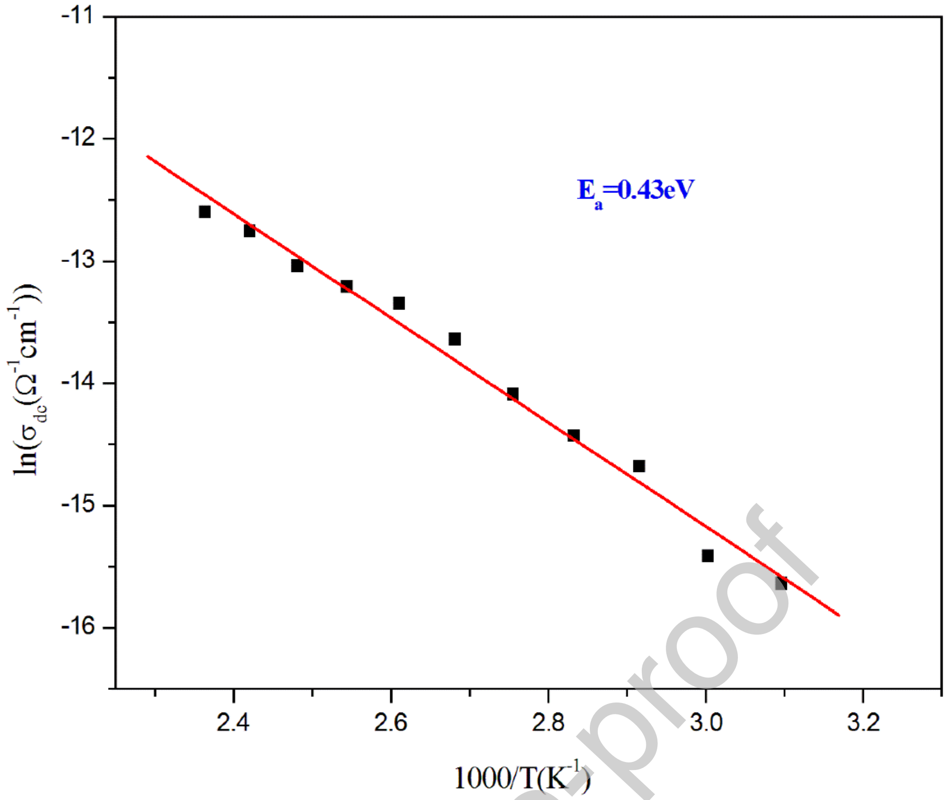

Figure 10: Variation of the σ_{dc} versus 1000/T of [(R)-$C_5H_{14}N_2$]$PdCl_4$ (1).

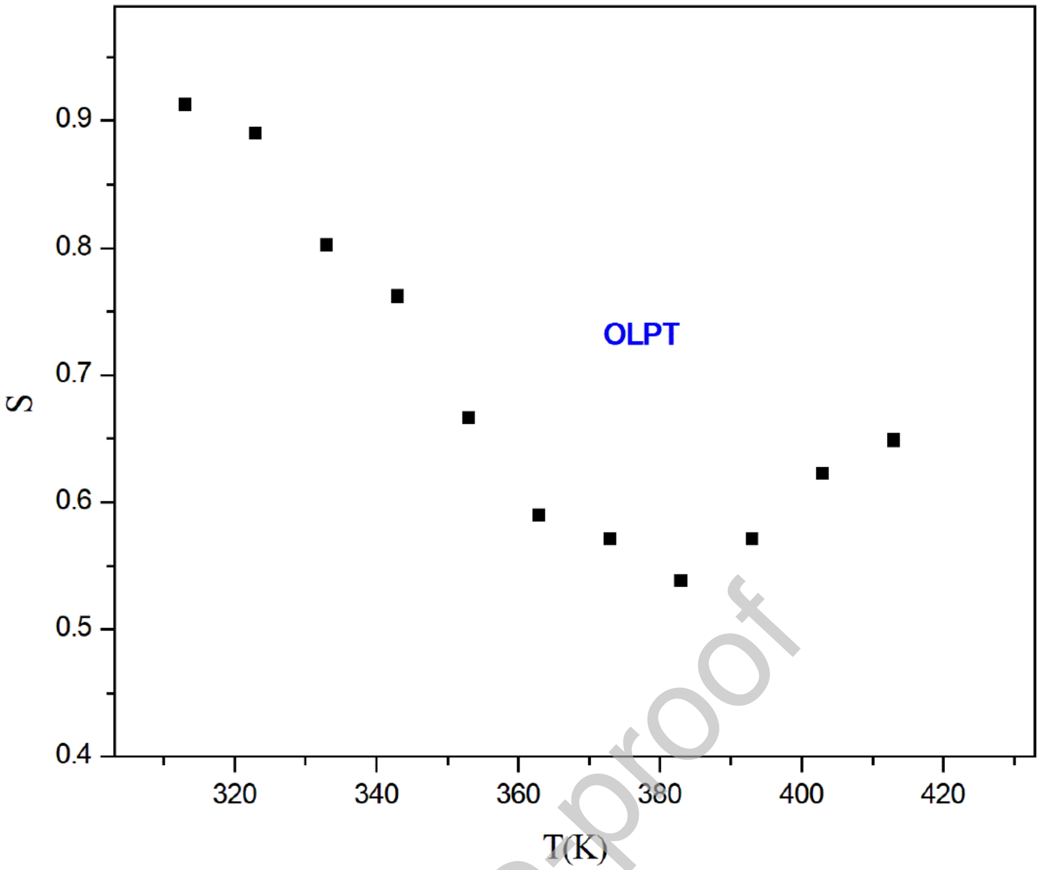

Figure 11: Variation of the exponent (S) versus temperature of [(R)-$C_5H_{14}N_2$]$PdCl_4$ (1).

Table 1. Crystallographic data for [(R)/(S)-$C_5H_{14}N_2$]$PdCl_4$ compounds.

Compound	[(R)-$C_5H_{14}N_2$]$PdCl_4$ (**1**)	[(S)-$C_5H_{14}N_2$]$PdCl_4$ (**2**)
Empirical formula	$C_5H_{14}Cl_4N_2Pd$	$C_5H_{14}Cl_4N_2Pd$
Formula weight (g.mol^{-1})	350.38	350.38
Temperature (K)	150	150
Crystal system	Orthorhombic	Orthorhombic
Space group	$P2_12_12_1$ (No. 19)	$P2_12_12_1$ (No. 19)
a (Å)	7.3659(14)	7.3663(10)
b (Å)	7.8775(17) Å	7.8582(10)
c (Å)	20.407(4)	20.414(3)
α (°), β (°), γ (°)	90	90
V (Å^3)	1184.1(4)	1181.7(3)
Z	4	4
ρ_{calc}, (g.cm^{-3})	1.965	1.969
Absorption correction	multi-scan	multi-scan
λ (Å)	0.71073	0.71073
μ (mm^{-1})	2.425	2.430
Crystal size (mm^3)	0.17*0.21*0.25	0.12*0.16*0.22
Crystal color/Shape	Orange/Prism	Orange/Prism
F (000)	688	688
θ range [°]	2.772 to 27.502	1.995 to 27.487
Collected reflections	12049	11220
Unique reflections	2710	2694
Observed data [I > 2.0 σ (I)]	2680	2672
R int	0.030	0.049
R1, wR2 [I > 2σ(I)]	0.0170, 0.0403	0.0213, 0.0504

R1, wR2 [all data]	0.0172, 0.0404	0.0215, 0.0505
Goodness-of-fit	1.13	1.10
Flack parameter	-0.011(14)	-0.026(19)
Largest difference map peak and hole (e. Å^3)	-0.38 / 0.59	-0.81 / 0.44

Author statement

- These are the standard contribution roles:

- **Conceptualization:** Hajlaoui Fadhel; Karim Karoui, Nathalie Audebrand
- **Data curation :** Bochra Ben Salah, Thierry Roisnel, Karim Karoui, Stéphane Freslon, Fathi Jomni
- **Formal analysis:** Hajlaoui Fadhel, Karim Karoui, Nabil Zouari
- **Funding acquisition:** Nabil Zouari, Fathi Jomni
- **Investigation:** Hajlaoui Fadhel, Nathalie Audebrand, Karim Karoui
- **Methodology:** Hajlaoui Fadhel
- **Project administration:** Fathi Jomni, Karim Karoui
- **Resources:** Fathi Jomni, Nabil Zouari
- **Software:** Bochra Ben Salah
- **Supervision :** Hajlaoui Fadhel, Nathalie Audebrand
- **Validation:** Karim Karoui, Nathalie Audebrand
- **Visualization :** Hajlaoui Fadhel, Karim Karoui
- **Roles/Writing – original draft :** Bochra Ben Salah
- **Writing – review & editing:** Hajlaoui Fadhel, Nathalie Audebrand, Karim Karoui.

The submission of the manuscript has been approved by all co-authors.

CONFLICT OF INTEREST

NOne

Graphical Abstract

Graphical Abstract:

Enantiomorphic organic–inorganic palladium halides induced by chiral organic cations exhibit semiconducting properties.